Stereotactic and Functional Neurosurgery

Stereotact Funct Neurosurg , DOI: 10.1159/000549229
Received: December 14, 2024
Accepted: October 21, 2025
Published online: October 27, 2025

# Imaging changes and Clinical outcome after MR-guided Laser Interstitial Thermal Therapy

Bergman L, Agur A, Gabay S, Tankus A, Strauss I, Zach L, Aizenstein O, Grossman R, Shahar T, Strauss I

ISSN: 1011-6125 (Print), eISSN: 1423-0372 (Online)
https://www.karger.com/SFN
Stereotactic and Functional Neurosurgery

Imaging changes and Clinical outcome after MR-guided Laser Interstitial Thermal Therapy

Lottem Bergman[1], Ariel Agur[1], Segev Gabay[1], Ariel Tankus[1,4,5], Itai Strauss[4], Leor Zach[2,5], Orna Aizenstein[3,5], Rachel Grossman[6,7], Tal Shahar[1], Ido Strauss[1,5]

1. Department of Neurosurgery, Tel-Aviv Medical Center, Tel-Aviv, Israel.
2. Oncology Institute, Tel-Aviv Medical Center, Tel-Aviv, Israel.
3. Department of Radiology, Tel-Aviv Medical Center, Tel-Aviv, Israel
4. Sagol School of Neuroscience, Tel Aviv University, Tel Aviv, Israel.
5. Gray Faculty of Medicine, Tel-Aviv University, Tel Aviv, Israel.
6. Brain Tumor Center, Department of Neurosurgery, Rambam Health Care Campus Rappaport Faculty of Medicine, Haifa, Israel.
7. Technion - Israel Institute of Technology, Haifa, Israel.

Corresponding Author: Ido Strauss
E-mail address: idos@tlvmc.gov.il

Abstract
Introduction
MR-guided laser interstitial thermal therapy (MRgLITT) is a minimally invasive technique for treating deep-seated brain lesions. However, the dynamics of imaging changes that occur after the ablation are not well characterized. This study aims to describe the clinical outcomes and volume changes that occur over time after MRgLITT.

Methods
We retrospectively collected clinical and imaging data of all adult patients who underwent MRgLITT of brain tumors (primary and metastatic) between 01/2020-06/2024. Volumes and diameters of the lesions were measured on gadolinium-enhanced T1-weighted images using Brainlab Elements. Local control was assessed at the last follow-up.
Results
Twenty-nine patients with 32 treated lesions were available for assessment. Most lesions (n=21) were metastatic, while 11 lesions were gliomas. The mean follow-up period was 23.4±13.1 months. The average preoperative tumor volume was 2.8±1.8cc. Post-ablation, the lesions' volumes increased on average by 250% (up to 450%) in the first month after surgery compared to the preoperative volumes. The enhancing ring extended distally beyond the tip of the catheter for an average of 4.5±1.8 mm. Glial lesions had a median progression-free survival of 8.5 months. The volume of metastatic lesions decreased below the preoperative volume on average 3 months after surgery. Local control was achieved in 16 of 21 metastatic lesions (76%) and was significantly better for lesions smaller than 4cc in volume and 16mm in maximal diameter that could be completely covered by the thermal damage estimate (TDE). Nodular enhancement at 3 months post-surgery was correlated with local failure.
Conclusion
MRgLITT can achieve good local control in metastatic brain lesions and should be considered early during follow-up after radiosurgery when local failure is suspected. The enhancing lesion extends beyond the tip of the catheter and enlarges during the first month post-ablation before gradually decreasing in size. Failure to decrease in size after 3 months or appearance of a nodular enhancement should raise suspicion of local failure.

## Introduction

MR-guided laser interstitial thermal therapy (MRgLITT) is an increasingly accepted minimally invasive treatment method for various brain lesions, including both primary and metastatic tumors and epileptogenic lesions(1–4). It utilizes laser-induced thermal energy to ablate abnormal tissue, making it particularly useful for deep-seated brain lesions where the surgical approach is associated with potential neurological morbidity. Retrospective studies have suggested that MRgLITT is a safe and effective minimally invasive treatment option for high-grade gliomas(2,5,6), metastatic lesions(7,8), and radiation necrosis(9,10). However, Imaging follow-up after MRgLITT for tumors can be challenging due to contrast enhancement of the ablated tissue that cannot be readily differentiated from the enhancing tumor. Thus, imaging dynamics are not always clear, making it sometimes difficult to determine treatment success or failure(11–17). Lesion imaging dynamics have been previously described in the literature, with most studies reporting an initial increase in lesion size on T1 with contrast after the ablation, followed by a decrease in size. However, reported follow-up times are short (several months), and the study cohorts are relatively small. Clinical outcomes vary for metastatic lesions, where good local control can be achieved depending on the shape and size(9,18–20) and for glial lesions, where progression-free survival is usually limited due to the infiltrative nature of gliomas(21–23).

Our study aims to enhance the understanding of imaging changes that occur during long-term follow-up after MRgLITT for tumors and to assist in clinical decision-making. We assess the correlation between the Thermal Damage Estimation (TDE) model of the VISUALASE system (Medtronic) and the enhancing volume on immediate postoperative MRI scans, including the extent of ablation beyond the catheter tip. This information can optimize MRgLITT. Furthermore, we developed a new method for estimating the ablated volume.

## Methods

### Patient selection

We conducted a retrospective analysis of clinical data from all adult patients (aged >18 years) who underwent MRgLITT for tumor ablation between 01/2020 and 06/2024. The study was approved by our Tel Aviv Medical Center review board (approval number IRB 0279-24).

### Operative technique

MRgLITT was performed as described previously(1). Briefly, preoperative MRI (MPRAGE with gadolinium) was fused to a stereotactic CT performed on the day of surgery using either Brainlab Elements (Munich, Germany) or ROSA software (MedTech, France). Stereotactic placement of the VISUALASE catheter (Medtronic Inc., Dublin, Ireland) to the predefined target was performed in the OR using either the Leksel G-frame (before July 2021) or ROSA ONE Brain robot. In this study, we only used the 10mm tip fiber. Patients were then transferred to the MRI suite for the actual ablation. Ablations were performed under real-time, 2-plane MR thermometry in a 1.5T scanner (Philips Ingenia MR-RT XD). T1-weighted images were acquired using a 3D MPRAGE sequence in the axial plane with isotropic 1 $mm^3$ resolution. Sequence parameters: TR = 2000 ms, TE = 2.38 ms, TI = 920 ms. Biopsies were not routinely performed. Immediate post-operative gadolinium-enhanced MRI was performed at the end of the ablations.

### Data collection

We extracted demographic, clinical, and outcome data from electronic medical records. Lesion parameters, including volume and maximal diameters, were measured using Brainlab Elements (Munich, Germany) on T1-weighted contrast-enhanced (MPRAGE) MR images. Usually, imaging was performed on the week before surgery, immediately after surgery, at 1 month, 3 months, and then every 3 months. In this study, we focused only on the T1-weighted contrast-enhanced series to evaluate volume changes. Some patients were also scanned 1 week after surgery. Local failure was defined as a lesion that failed to decrease in size after 3-6 months or showed nodular enhancement (Figure 1). As this is a retrospective study, there is some non-uniformity in the follow-up intervals.

### Dimensions of the thermal damage estimation model

We implemented in MATLAB (Mathworks, Natick, MA) the procedures of Liang et al(24). for estimating the ablation dimensions in magnetic resonance-guided laser interstitial thermal therapy. In brief, the user marked a loose rectangle around the thermal damage and the laser catheter in a brightened version of the post-operative TDE image. The marked area was then magnified for more accurate manual marking. On the magnified image, the user marked two points along the laser catheter, starting with the one farther away from the thermal damage. These points determined the laser catheter line. The algorithm found the entry and exit points of this line to the thermal damage area and calculated the distance between these points. We then computed a perpendicular to this line via the midpoint of the entry and exit points and found its intersection with the edges of the thermal

damage. This procedure was repeated for the TDE images of both orthogonal planes. Next, the TDE images were rotated so that the laser catheter is parallel to the axes, to align the images. We then estimated elliptic cross-sections parallel to the second MRI image. The integral, i.e., the sum of total areas, of these cross-sections estimates the volume of the ellipsoid approximating the damaged brain volume. We calculated two estimates of this volume, one based on defining the minor axis based on averaging 4 sampled points on the ellipse of the first MRI image, and the other based on the maximum of these 4 points. These are models A and B of Liang et al.(24).
The volume estimates were normalized by the brain volume that each pixel represents, to reflect volume in cc.
In addition, we developed and implemented a new method for volume estimation, which we named the quarters model (Figure 2). This method estimates the areas of cross-sections along the major axis. Each such cross-section is perpendicular to both MRI images, so it intersects each at a single line. We therefore estimated this intersection line segment from each image. In practice, this segment may not be exactly centered at the intersection of the two MR images. This resulted in 4 estimations of the semi-axes of the cross-section ellipse. However, rather than estimating the cross section by a single ellipse, we approximated its area assuming there are 4 quarters-of-an-ellipse. The sum of the areas of each quarter-of-an-ellipse served as the estimation of the cross-section area for the computation of the volume. This computation is the same as the average area of the four ellipses formed by the two approximations of the semi-major axis combined with two of the semi-minor one.
For each method, we calculated the correlation coefficient between the measured volume and the estimated volume.

Statistical analysis

All statistical analyses were guided by a professional consultant and conducted using SPSS (IBM Corp., Version 29.0.2.0(20)). A p-value of less than 0.05 was considered statistically significant.

Results

Patient Characteristics

Twenty-nine patients underwent 32 MRgLITT procedures for ablation of 32 tumors between 01/2020 and 06/2024. Individual patients' data are given in Table 1; 18 patients were females (56%), and the median age was 61 years (range 24-78 years). Brain metastases after failure of radiosurgery accounted for 21 of the cases, with non-small cell lung cancer (NSCLC) and breast carcinoma being the most common etiologies (n=9 and n=6, respectively). Glial tumors accounted for 11 cases (Table 1). Median Karnofsky performance scale (KPS) at surgery was 80 (range 50-100).
The average clinical follow-up time was 23.4±13.1 months (range, 4-56 months; the minimal follow-up time was in a metastatic breast patient who passed away 5 months after surgery), and radiological follow-up was 21.8±13.8 months (range, 3.8-57.5 months). The median survival after MRgLITT for all glial tumors was 22.7 months (range 9-57 months; Figure 3; Table 1 for individual patients' pathology). For metastatic lesions, the median survival was not reached; The 12-month and 24-month overall survival rates were 85% (95% CI: 70–100%) and 81% (95% CI: 64–97%), respectively. prolonged steroid treatment for 2-8 weeks. The decision to continue the steroid treatment was made according to the imaging and the patient's clinical condition.
The mean preoperative tumor volume ($V_{pre}$) was 2.8±1.8 cc (range 0.9-7.9 cc), and the mean preoperative maximal diameter was 16.4±3.5mm (range 11.7-23.3mm). In each procedure, a single 10mm tip laser fiber was used through a single trajectory. During most surgeries (n=22), the ablation continued until the TDE model was judged to completely encompass the lesion on both monitored planes. In 10 cases, the ablation procedure was stopped without achieving complete ablation, either because the TDE did not enlarge any further (n=9) or in one awake case with the first signs of motor weakness in the hand. At the end of the ablation, a contrast-enhanced MRI was acquired to verify the ablation volume. The mean postoperative volume ($V_{post}$) was 5.23±2.65cc (range 1.66-11.8 cc), which was significantly larger than the $V_{pre}$ ($p<0.001$, Wilcoxon rank-sum test).

Damage model estimate validation

As the ablation was usually stopped once the TDE covered the entire preoperative lesion on the two monitored planes, we wondered why the $V_{post}$ was significantly bigger than $V_{pre}$. We decided to test whether the difference between $V_{post}$ and $V_{pre}$ was due to over-ablation or underestimation of the TDE of the actual ablation.
Therefore, we calculated an estimate of the 3-D ablation volume from the two 2-D TDE ($V_{TDE}$) and compared this extrapolated volume to the "real" $V_{post}$ of the lesions contoured manually on Brainlab Elements. The extrapolated TDE volumes were calculated using three different methods (methods A&B according to Liang et al (18), and our Quarters method; Figure 2). We found that $V_{post}$ was significantly larger than $V_{TDE}$ calculated using all 3 methods ($P<0.001$, Wilcoxon test). When we examined the immediate post-ablation scans, we noticed that the ablated lesions were characterized by a thick enhancing ring surrounding a weakly enhancing center (Figure 4A). As $V_{post}$

was contoured along the outer circumference of the enhancing rim, we decided to additionally contour the lesions along the inner border of the enhancing rim ($V_{in}$; Figure 4B). We then compared $V_{in}$ to the extrapolated $V_{TDE}$ using the different methods and found a moderate correlation with both our Quarters method (r = 0.686, Spearman's correlation) and Liang's Models (Model A: r = 0.644, Model B: r = .0659, Spearman's correlation).

Distal extension of the thermal damage:

The length of the enhancing postoperative lesions created along the axis of the optic fiber is highly variable and depends on the number of "pullbacks" performed during the procedure. We noticed that the lesions usually extended in a distal direction beyond the tip of the catheter (Figure 5). We measured this distal extension on T1-enhanced images. The distal extension created by the VISULASE 10mm catheter was 4.5±1.8mm (n=28; in 4 lesions, the tip of the catheter was placed beyond the lesion and the optic fiber was retracted within the catheter before the first ablation).

Volume changes over time:

Lesions' volume changes were evaluated on serial follow-up imaging. For each patient, all available follow-up scans were uploaded to Brainlab Elements, and lesions were contoured on contrast-enhanced T1, allowing direct measurement of volumes at each time point. Due to the different clinical courses of glial tumors and metastases, we divided the results into two separate groups.

Metastases volume dynamics:

The average preoperative volume of the treated metastases (n=21) was 2.8±1.5cc (median 2.4cc, range 0.9-6.7 cc). The immediate mean postoperative volume of the outer ring enhancement ($V_{post}$) was 4.9±2.3cc, while $V_{in}$ was 2.5±1.5cc.

At follow-up, the thickness of the enhancing ring decreased, and we continued to measure only a single volume of the entire enhancing lesion. To allow comparisons, postoperative volumes were normalized to the preoperative volumes. There was an initial increase in the mean volume to 251±71% (n=10) and 199±96%(n=19) after 1 week and 1 month, respectively. Volume then decreased to 109±49%(n=17) after 3-months, and 67±41%(n=18) after 6-months, with further gradual decrease over time to 47±29%(n=14), 36±31%(n=14), 19±17%(n=13) and 19±23%(n=9 after 9,12,18 and 24 months respectively (Figure 6).

Glial tumors volume dynamics:

The average preoperative volume of glial tumors (n=11) was 2.87±2.21cc, and the immediate postoperative $V_{post}$ and $V_{in}$ were 5.5±3cc and 3.15±1.7cc, respectively. At follow-up, the average normalized volume after one week was 416±143% (n=3), and after 1 month, 244±145%(n=6). Volumes then gradually decreased to 203±128%(n=10), 278±348% (n=8), 143±142% (n=9) and 197±117% (n=3) after 3,6,9 and 12 months respectively (Figure 7).

Local Control:

We found a significant relationship between the complete coverage of the tumor by the TDE and local control ($p<0.001$, Log Rank). Out of the 10 lesions that were not completely ablated (i.e., not entirely covered by the TDE, example shown in Figure 8), 8 resulted in local failures. However, out of the 22 lesions that were completely ablated, only two local failures were observed, both of which were glial tumors.

Local control in metastases:

In 16 out of 21 cases, local control was maintained at the last imaging follow-up (median 21 months, range 3-52 months). In all 5 cases of failure, the TDE did not encompass the entire tumor on one or both monitored planes at the end of the procedure (Figure 8), although the postoperative volume ($V_{post}$) was larger than the preoperative volume. The median time to failure in these cases was 3.9 months (range 3.2-6.4 months).

Nodular enhancement was seen in 6 out of the 21 metastatic lesions at 1 to 3 months post-ablation (Figure 1). Five of these cases (83.3%) progressed to local failure ($p < 0.001$, Fisher's Exact Test as a nested case-control study). Only one case that showed nodular enhancement resolved during follow-up.

Metastases' pre-op volume was significantly correlated to the risk of local failure with a hazard ratio of 2.37 ($p = 0.028$, Cox regression). There was an increased risk of local failure for lesions bigger than 4cc ($p=0.001$, Log Rank). We found that metastatic lesions larger than 16 mm in maximal diameter had an increased risk of local failure ($p = 0.021$, Log Rank). The average diameter of metastases that failed MRgLITT was 18.3mm±1.8mm (median 17.8mm, range 16.5-21.5mm).

Local control in glial tumors:

During the follow-up period (median 10.6 months), we observed 5 local failures in the group of 11 glial tumors. The median progression free survival was 8.5 months (range 2.8-34 months). Two of the failures were in cases

that were considered “complete” ablation. Of course, due to the infiltrative nature of glial tumors, the failure rate is expected to be high, the time to failure in the “completely” ablated cases (15.5 months) was longer than in the incomplete ablated cases (4.8 months).

Complications

In two cases, a small intra-lesional hemorrhage was observed at the end of the ablation that was not seen on the first MRI scan and was confirmed with susceptibility-weighted imaging (SWI) at the end of the lesioning. Both procedures were completed as planned without new neurological deficits. The patients were managed conservatively and discharged home 2 days later. Two patients with metastases in the primary sensory cortex developed sensory ataxia postoperatively. One patient who underwent awake MRgLITT for a metastasis in the motor cortex developed mild hand weakness upon which the ablation was stopped. The patient gradually improved during follow-up and retained local control 18 months after surgery.

Discussion

The current work describes the MR imaging characteristics and changes that occur over time after MRgLITT for brain tumors. Several interesting findings are described. First, we show that the immediate postoperative volumes of the enhancing lesions are significantly larger than the preoperative tumor volumes. This finding is in agreement with previous reports(13,14,25,26). Two explanations might account for this difference. The first might be due to an attempt to achieve complete ablation of the tumors and mild over-coverage of the tumor by the TDE. The second may be because the TDE model gives an underestimation of the enhancing lesion observed immediately post-ablation. The difference between the outer and inner volumes of the enhancing lesion ($V_{post}$ and $V_{in}$) represents the volume of the enhancing rim. This enhancing rim is an area where the blood-brain barrier (BBB) is disrupted(27–29) and may represent a transition zone between ablated and not ablated tissue. This observation concurs with previous reports describing different zones after ablation and a discrepancy between TDE and the post-op volume (12,13,25,26). Of note is that Medtronic recently updated the Visualase software to accommodate this transition zone; however, during the study period, we still used the previous version of the software.

We also demonstrated that the lesions created using the 10mm Visulase tip extend, on average, 4.5 mm distally from the catheter tip. This information is important in planning the depth of the target needed to achieve complete ablation without damaging surrounding healthy neural tissue. It can also be used as a safety distance to keep the sharp tip of the cooling catheter away from blood vessels without compromising the ablation.

The optimal salvage treatment for local recurrence of brain metastases after initial radiosurgery is not well defined. Local failure is often due to a radioresistant tumor, so lower doses of re-irradiation are unlikely to achieve long-term disease control. A recent review found a 72.5% local control rate at 1 year that dropped to 54% at 2 years after re-radiosurgery for brain metastasis. In addition, there was an increased risk of symptomatic radiation necrosis in 13% of the cases(30). Open resection is typically reserved for selected cases and is associated with increased risks, especially in cases of deep-seated lesions.

MRgLITT provides cytoreduction in cases of recurrent tumor and also effectively ablates necrotic tissue, thereby relieving mass effect and reducing perilesional edema(9). The maximum size of lesions that can be created using MRgLITT is not well established and probably depends on both tissue properties and the laser wavelength used. In the current study we used exclusively the Medtronic Visualase system which uses a 980nm laser and according to the published literature can effectively ablate lesions with a diameter up to 18-20 mm(9,31,32). Local control in our cohort was correlated with the complete coverage of the tumor by the TDE model and was particularly good for metastatic lesions smaller than 16mm in maximal diameter and 4cc in volume. Similar findings were recently reported by Sanvito et al. and Bastos et al., who described cut-offs of 2.5 cc and 6 cc, respectively(31,32). Of note, according to the literature the Monteris system which uses a 1064nm laser may achieve deeper tissue penetration and ablate lesions up to 3 cm in maximal diameter(18,31). All the metastatic lesions in our series were treated with MRgLITT as a salvage therapy after the failure of radiosurgery. For these cases, MRgLITT offers a minimally invasive treatment with a low complication rate. Since local control was better for smaller lesions(13) we suggest that MRgLITT should be considered early when tumor regrowth is observed after radiosurgery, even before lesions become symptomatic.

Understanding the dynamics of post-operative imaging is important in making informed clinical decisions. In concordance with previous reports(2,6,11,14,15,17,33), we found that the volume of the post-operative enhancing lesion usually increases up to 4 times in size compared to the preoperative lesion, and begins to shrink only a month after, returning to the preoperative volume between 3-6 months after the MRgLITT procedures. Most of the available data are derived from small, heterogeneous cohorts with limited longitudinal follow-up, ranging from 3 to 24 months (4,11,13–17,38). Few studies like Basotos et al. (2020), Gurses et al (2024) and Haskell-Mendoza (2024) have systematically correlated radiological changes with clinical outcomes (20,33). This findings mean that although most lesions may increase in size during the initial follow-up, continued growth after 3-6 months should raise suspicion for local failure. This is in contrast to MRI changes after radiosurgery, where most lesions initially stabilize or shrink in size, and only 10-30% show a delayed increase in volume after 6-12 weeks termed “pseudo progression”(34–36). As many centers don’t routinely scan patients one month after MRgLITT, but rather 3-4 months postoperatively, we suggest that failure to return to preoperative size after 6 months should prompt retreatment or at least close observation. Especially, the appearance of a nodular enhancement within the ablated lesion during follow-up should raise suspicion for local recurrence.

A relevant question is whether tissue diagnosis via biopsy is necessary prior to MRgLITT to differentiate recurrent tumor from radiation necrosis. Differentiation between active tumor and radiation necrosis is challenging on

imaging studies alone due to their overlapping radiographic appearance(37). Tissue diagnosis can be obtained either in a staged procedure or in the same operative setting. If the biopsy is performed in a separate setting, it will subject the patient to two surgical procedures and delay definitive treatment. If performed in the same setting with MRgLITT, there is a small risk of intra-tumoral hemorrhage that can induce artifacts and interfere with the accuracy of the thermal maps during the ablation(1). In our institutional practice we forgo biopsy in most cases of previously irradiated metastases with clear imaging progression, as we believe that for patients with an expanding radiographic lesion, definitive treatment with LITT is indicated regardless of whether the underlying process is neoplastic or necrotic. However, it is important to acknowledge that tissue diagnosis may provide valuable information. In particular, it can reveal genetic/molecular transformation to guide further treatment. Thus, while our approach minimizes procedural risk and delay in cases with clear clinical and radiographic indications for ablation, the potential diagnostic value of biopsy should be recognized in cases where imaging is equivocal or management would be altered by the histopathological findings.

Study limitations

Our study has several limitations. First, the relatively small sample size may limit the generalizability of our findings. Second, the patients included in the study had various pathologies, and some of these conditions involved systemic treatments that were not accounted for, potentially affecting the interpretation of the results. Moreover, due to the lack of biopsy, we can't be sure that the imaging changes are not related to radiation necrosis. Third, imaging was performed using different devices, introducing measurement variability. Finally, the lack of uniformity in imaging follow-up, with some lesions receiving more frequent imaging than others, could impact the assessment of treatment response over time.

Conclusions

MRgLITT achieves good local control, especially for small metastatic lesions, and should be considered early during follow-up after radiosurgery when local failure is suspected. Failure to achieve complete tumor coverage by the TDE predicted local failure and should, therefore, prompt closer observation during follow-up. Postoperatively, lesions may initially enlarge up to 4 times the preoperative volume, returning to being below the preoperative volume within 3 to 6 months. Differentiating between expected imaging changes and local failure can be challenging and further studies using advanced imaging are needed to better differentiate between the two conditions.

Acknowledgments:

The authors would like to thank Prof. Tomer Ziv-Baran for his assistance with the statistical analysis.

Statement of Ethics:

We confirm that we have read the Journal's position on issues involved in ethical publication and affirm that this report is consistent with those guidelines.

The study was approved by our Tel Aviv Medical Center review board (approval number IRB 0279-24), and has been granted a waiver from requiring written informed consent.

Conflict of Interest Statement:

Ido Strauss received speaker honoraria from Medtronic. None of the other authors has any conflict of interest to disclose.

Funding Sources:

There was no funding for this paper.

Author Contributions

LB: Investigation, Visualization, Writing – original draft. AA: Writing – review & editing, SG: Writing – review & editing. AT: Methodology, Formal analysis, Writing – review & editing. IS: Methodology. LZ: Writing – review & editing, Resources. OA: Writing – review & editing, Resources. RG: Writing – review & editing, Resources. TS: Writing – review & editing, Resources. IS – Conceptualization, Supervision, Writing – original draft, Writing – review & editing.

Data Availability:

The data supporting this study's findings is not publicly available due to patient privacy but is available from LB (lottemb@gmail.com) upon reasonable request.

References


1. Shofty B, Bergman L, Berger A, Aizenstein O, Ben-Valid S, Gurovich D, et al. Adopting MR-guided stereotactic laser ablations for epileptic lesions: initial clinical experience and lessons learned. Acta Neurochir (Wien). 2021 Oct;163(10):2797–803.
2. Carpentier A, Chauvet D, Reina V, Beccaria K, Leclerq D, McNichols RJ, et al. MR-guided laser-induced thermal therapy (LITT) for recurrent glioblastomas. Lasers Surg Med. 2012 Jul;44(5):361–8.
3. Grossman R, Strauss I. [laser interstitial thermal therapy (litt) in neurosurgery]. Harefuah. 2023 Feb;162(2):110–5.
4. Hawasli AH, Bagade S, Shimony JS, Miller-Thomas M, Leuthardt EC. Magnetic resonance imaging-guided focused laser interstitial thermal therapy for intracranial lesions: single-institution series. Neurosurgery. 2013 Dec;73(6):1007–17.
5. Mohammadi AM, Hawasli AH, Rodriguez A, Schroeder JL, Laxton AW, Elson P, et al. The role of laser interstitial thermal therapy in enhancing progression-free survival of difficult-to-access high-grade gliomas: a multicenter study. Cancer Med. 2014 Aug;3(4):971–9.
6. Patel PD, Patel NV, Danish SF. The Evolution of Laser-Induced Thermal Therapy for the Treatment of Gliomas. Neurosurg Clin N Am. 2023 Apr;34(2):199–207.
7. Sabahi M, Bordes SJ, Najera E, Mohammadi AM, Barnett GH, Adada B, et al. Laser Interstitial Thermal Therapy for Posterior Fossa Lesions: A Systematic Review and Analysis of Multi-Institutional Outcomes. Cancers (Basel). 2022 Jan 17;14(2).
8. Sharma M, Do TH, Palzer EF, Huling JD, Chen CC. Comparable safety profile between neuro-oncology procedures involving stereotactic needle biopsy (SNB) followed by laser interstitial thermal therapy (LITT) and LITT alone procedures. J Neurooncol. 2023 Mar 15;162(1):147–56.
9. Rao MS, Hargreaves EL, Khan AJ, Haffty BG, Danish SF. Magnetic resonance-guided laser ablation improves local control for postradiosurgery recurrence and/or radiation necrosis. Neurosurgery. 2014 Jun;74(6):658–67; discussion 667.
10. Scherschinski L, Jubran JH, Shaftel KA, Furey CG, Farhadi DS, Benner D, et al. Magnetic Resonance-Guided Laser Interstitial Thermal Therapy for Management of Low-Grade Gliomas and Radiation Necrosis: A Single-Institution Case Series. Brain Sci. 2022 Nov 28;12(12).
11. Xue Z, Guan X, Yuan L, Kang P, Zhang C, Li D, et al. Laser interstitial thermal therapy in the treatment of brain metastases: the relationship between changes in postoperative magnetic resonance imaging characteristics and tumor recurrence. Acta Neurochir (Wien). 2023 May;165(5):1379–87.
12. Patel NV, Frenchu K, Danish SF. Does the thermal damage estimate correlate with the magnetic resonance imaging predicted ablation size after laser interstitial thermal therapy? Oper Neurosurg (Hagerstown). 2018 Aug 1;15(2):179–83.
13. Beechar VB, Prabhu SS, Bastos D, Weinberg JS, Stafford RJ, Fuentes D, et al. Volumetric response of progressing post-SRS lesions treated with laser interstitial thermal therapy. J Neurooncol. 2018 Mar;137(1):57–65.
14. Patel NV, Jethwa PR, Barrese JC, Hargreaves EL, Danish SF. Volumetric trends associated with MRI-guided laser-induced thermal therapy (LITT) for intracranial tumors. Lasers Surg Med. 2013 Aug;45(6):362–9.
15. Eichberg DG, VanDenBerg R, Komotar RJ, Ivan ME. Quantitative Volumetric Analysis Following Magnetic Resonance-Guided Laser Interstitial Thermal Ablation of Cerebellar Metastases. World Neurosurg. 2018 Feb;110:e755–65.
16. Merenzon MA, Levy AS, Bhatia S, Rivera C, Morell AA, Semonche A, et al. Towards the definition of progressive disease in brain metastasis treated with laser ablation: an evidence-based study. J Neurooncol. 2023 Jun 12;163(2):463–71.
17. Sanvito F, Yao J, Nocera G, Shao G, Wang Z, Cho NS, et al. Volumetric and diffusion MRI longitudinal patterns in brain metastases after laser interstitial thermal therapy. Eur Radiol. 2025 Apr 18;
18. Salehi A, Kamath AA, Leuthardt EC, Kim AH. Management of intracranial metastatic disease with laser interstitial thermal therapy. Front Oncol. 2018 Oct 31;8:499.
19. Alattar AA, Bartek J, Chiang VL, Mohammadi AM, Barnett GH, Sloan A, et al. Stereotactic Laser Ablation as Treatment of Brain Metastases Recurring after Stereotactic Radiosurgery: A Systematic Literature Review. World Neurosurg. 2019 Aug;128:134–42.
20. Gurses ME, Lu VM, Gecici NN, Gökalp E, Shah KH, Metzler AR, et al. Laser interstitial thermal therapy in neurosurgery: a single-surgeon experience of 313 patients. J Neurosurg. 2024 Nov 1;141(5):1281–91.

21. Khalafallah AM, Shah KH, Knott MV, Berke CN, Shah AH, Komotar RJ, et al. Evaluating laser interstitial thermal therapy for newly diagnosed, deep-seated, large-volume glioblastoma: survival and outcome analysis. Neurosurg Focus. 2024 Nov 1;57(5):E3.
22. O'Halloran PJ, Henry J, Amoo M, Kalyvas A, Mohan N, Zadeh G, et al. LITTing up Gliomas-Is the Future Bright? World Neurosurgery: X. 2023 Jan;17:100136.
23. Seaton MP, Schmidt JC, Brown NJ, Sahyouni R, Khalessi AA, Ben-Haim S, et al. Contemporary applications of laser interstitial thermal therapy: A comprehensive systematic review. World Neurosurg. 2025 Jan;193:356–72.
24. Liang AS, Munier SM, Danish SF. Mathematical Modeling of Thermal Damage Estimate Volumes in MR-guided Laser Interstitial Thermal Therapy. J Neuroimaging. 2021 Mar;31(2):334–40.
25. Sundararajan SH, Belani P, Danish S, Keller I. Early MRI Characteristics after MRI-Guided Laser-Assisted Cingulotomy for Intractable Pain Control. AJNR Am J Neuroradiol. 2015 Jul;36(7):1283–7.
26. Atsina K-B, Sharan AD, Wu C, Evans JJ, Sperling MR, Skidmore CT, et al. JOURNAL CLUB: Longitudinal Qualitative Characterization of MRI Features After Laser Interstitial Thermal Therapy in Drug-Resistant Epilepsy. AJR Am J Roentgenol. 2017 Jan;208(1):48–56.
27. Bartlett S, Nagaraja TN, Griffith B, Farmer KG, Van Harn M, Haider S, et al. Persistent Peri-Ablation Blood-Brain Barrier Opening After Laser Interstitial Thermal Therapy for Brain Tumors. Cureus. 2023 Apr 10;15(4):e37397.
28. Morris S-A, Rollo M, Rollo P, Johnson J, Grant GA, Friedman E, et al. Prolonged Blood-Brain Barrier Disruption Following Laser Interstitial Ablation in Epilepsy: A Case Series with a Case Report of Postablation Optic Neuritis. World Neurosurg. 2017 Aug;104:467–75.
29. Patel B, Yang PH, Kim AH. The effect of thermal therapy on the blood-brain barrier and blood-tumor barrier. Int J Hyperthermia. 2020 Jul;37(2):35–43.
30. Lucia F, Touati R, Crainic N, Dissaux G, Pradier O, Bourbonne V, et al. Efficacy and safety of a second course of stereotactic radiation therapy for locally recurrent brain metastases: A systematic review. Cancers (Basel). 2021 Sep 30;13(19).
31. Sanvito F, Telesca D, Cho NS, Sayari JT, Nagaraj R, Raymond C, et al. Small pretreatment lesion size and high sphericity as favorable prognostic factors after laser interstitial thermal therapy in brain metastases. J Neurosurg. 2024 Feb 1;140(2):338–49.
32. Bastos DC de A, Rao G, Oliva ICG, Loree JM, Fuentes DT, Stafford RJ, et al. Predictors of local control of brain metastasis treated with laser interstitial thermal therapy. Neurosurgery. 2020 Jul 1;87(1):112–22.
33. Haskell-Mendoza AP, Reason EH, Gonzalez AT, Jackson JD, Sankey EW, Srinivasan ES, et al. Automated segmentation of ablated lesions using deep convolutional neural networks: A basis for response assessment following laser interstitial thermal therapy. Neuro Oncol. 2024 Jun 3;26(6):1152–62.
34. Patel TR, McHugh BJ, Bi WL, Minja FJ, Knisely JPS, Chiang VL. A comprehensive review of MR imaging changes following radiosurgery to 500 brain metastases. AJNR Am J Neuroradiol. 2011 Sep 15;32(10):1885–92.
35. Salbas A, Koc AM, Coskun M, Horoz EM, Sengul A, Gelal MF. Temporal evolution of MRI findings and survival outcomes in patients with brain metastases after stereotactic radiosurgery. BMC Med Imaging. 2025 May 14;25(1):161.
36. Romano A, Moltoni G, Blandino A, Palizzi S, Romano A, de Rosa G, et al. Radiosurgery for Brain Metastases: Challenges in Imaging Interpretation after Treatment. Cancers (Basel). 2023 Oct 21;15(20).
37. Chernov MF, Ono Y, Abe K, Usukura M, Hayashi M, Izawa M, et al. Differentiation of tumor progression and radiation-induced effects after intracranial radiosurgery. Acta Neurochir Suppl. 2013;116:193–210.
38. Tovar-Spinoza Z, Choi H. Magnetic resonance-guided laser interstitial thermal therapy: report of a series of pediatric brain tumors. J Neurosurg Pediatr. 2016 Jun;17(6):723–33.

Figure legends

Figure 1: Example of with and without local control over time

Figure 1: The upper panels (A-G) show a lesion that exhibited good local control over time with shrinkage of the lesion to below the pre-op volume at 6 months post-op. The lower panels (H-M) depict a lesion that showed nodular enhancement after 3 months (red arrow in K), which continued to grow at 6 months post-operatively (L) and was subsequently resected (M).

Figure 2: An example of the computations of the TDE from two cross-section MR images according to three methods: Ellipsoid, Liang *et al*. (2021), and Quarters model.

**Figure 2:** An example of the computations of the TDE from two cross-section MR images according to three methods: Ellipsoid, Liang *et al*. (2021), and Quarters model. **A.** The two MR images (Left). The user loosely drew a rectangle (red) around the thermal damage and the laser catheter and two points on the image of the canula. The point farther from the thermal damage is marked by a magenta cross and the nearer, by a cyan one (enlarged on the Right). These marks are extrapolated to find out the entry (green) and exit (red) points of the laser trajectory within the thermal damage area. We call the segment between these points: the major axis of the TDE. Then, the line perpendicular to the laser trajectory at the center of the major axis is estimated. Its ends within the thermal damage area are marked by blue and yellow crosses. The segment between these points is named: the minor axis of the TDE. **B.** A 3D plot of the MR images aligned according to the laser trajectory which appears in both. The major axis of the TDE is marked by a red line. The minor axes of the TDE in the XY and XZ planes are marked by blue and green lines, respectively. **C.** An enlarged 3D plot of the TDE with its major and minor axes as in (B). **D.** In the ellipsoid method, the major and minor axes of the TDE serve as the major and minor axes of an ellipsoid estimating the TDE. The volume of the magenta ellipsoid is the estimator of the TDE volume. Red thick arrows point to example areas of the TDE uncovered by the ellipsoid which are therefore not included in the computed volume. The cyan arrow indicates an example area of no thermal damage still included in the ellipsoid. **E.** Volume computation according to the method of Liang *et al*. (2021). The computation is based on the red ellipse at the XY plane. Its major axis is the TDE major axis. To compute its minor axis, four points along the edge of the TDE of the XY MR image are sampled, from which four estimates of the minor axis of the ellipse are calculated (not shown in the image): $a_1$, $a_2$, $a_3$, $a_4$. The average of these estimates, denoted $a_{avg}$, serves as the minor axis of the red ellipse. Now, the method iterates the minor axis of the red ellipse (which is in the direction of the blue line). From each point on the minor axis of the red ellipse, it calculates a line perpendicular to the axis in the XY plane, marked by black lines. This serves as the major axis of a magenta ellipse, which is parallel to the XZ plane. The minor axis of the magenta ellipse (vertical cyan line) is estimated by multiplying the major axis (black line) with a minor/major axes ratio characterizing the thermal damage in the XZ plane (computation not shown here). The sum of the areas of the magenta ellipses is the estimated TDE volume. Some inaccuracies in the estimated TDE are marked by red and cyan arrows, as in (D). **F.** The same as (E), but the minor axis of the red ellipse is estimated as the maximum of $a_1$, $a_2$, $a_3$, $a_4$, denoted: $a_{max}$. This decreases the thermal damage area not covered by the estimator (red arrows), but increases the areas of no damage still included in the computation (cyan ones). **G.** Illustration of the Quarters method – cross-section in the YZ plane. From each MR image we estimated two semi-axes: $a_1$ and $a_2$ from $im_1$ (the image at the XY plane), and $a_3$ and $a_4$ from $im_2$ (the image at the XZ plane). Note that these are completely different estimates from the ones in Liang *et al*. method, and in addition they estimate ellipses in the YZ plane, not the XZ plane as in Liang *et al*. Each quarter of this cross-section may thus have different estimations of its semi-axes. From each pair of adjacent estimations: ($a_1$, $a_3$), ($a_3$, $a_2$), ($a_2$, $a_4$), ($a_4$, $a_1$), we computed the area of the quarter-of-ellipse: $A_{quarter} = \frac{1}{4}\pi a_i\, a_j$ where $a_i$ and $a_j$ are the semi-axes of the quarter-of-ellipse. The total area of these four quarters-of-ellipse (i.e., the total area in all four tints of blue) served as our estimator for the cross-section area. **H.** The Quarters method. We iterate the major axis of the thermal damage (red line) and estimate the area of cross-sections parallel to the YZ plane (see (G)). In this cross-section, the edges of the actual thermal damage in each of the images are taken as estimates for the semi-axes (denoted $a_1$, $a_2$, $a_3$, $a_4$ in (G)). In each YZ plane, the area of four quarters-of-ellipse is estimated. The sum of these areas is the estimator of the TDE volume. As can be seen in the figure, the Quarters method refrains from inclusion of any non-damage area, and avoids exclusion of any thermal damage area in the images. The method utilizes all available information about the damaged volume, and is thus optimal under the assumption that unavailable damage volume should be approximated elliptically. **I.** & **J.** The Quarters method from two more viewpoints, demonstrating the accurate coverage of the available images of the thermal damage.

Figure 3: Survival curves

Figure 3: Kaplan-Meier curves for A – Metastatic lesions, B – Glial lesions. The Y-axis shows cumulative survival, and the X-axis shows time in months.

Figure 4: Lesions contouring and Thermal Damage Estimation

**Figure 4:** Demonstrative case (#2) showing the two different volume contouring options $V_{post}$ and $V_{in}$. A - immediate post-operative contrast-enhanced MRI. B – On the same scan, lesions were contoured using Brainlab Elements. $V_{post}$ was contoured along the outer border of the enhancing rim (yellow line); $V_{in}$ (blue line) was contoured along the inner border. C – The corresponding TDE is shown on a coronal MR image from the Visualase System.

Figure 5: distal extension of the Thermal Damage

**Figure 5.** A shows the immediate post-ablation T1+gadolinium MRI scan aligned using Brainlab elements aligned along the laser catheter. B - shows how the distal extension of the thermal damage was measured from the tip of the laser catheter (orange line) to the furthest point of the contrast enhancement.

Figure 6: Dynamics in Metastatic Lesions Volume

**Figure 6** presents the changes in volume of 21 different metastatic lesions that underwent MRgLITT. The black dashed line is the average. The Y-axis is the lesion volume normalized to pre-op volume, and the X-axis is the time of the imaging. Lesions grew significantly in the first month after surgery, and most decreased in size as time passed since surgery.

Figure 7: Dynamics in Glial Lesions Volume

**Figure 7** presents the change in volume of 11 different glial lesions that underwent MRgLITT. The black dashed line is the average. Y-axis is the lesion volume normalized to pre-op; X-axis is the imaging time.

Figure 8 – Thermal Damage Model Estimation Not Encompassing the Whole Lesion - An Example

**Figure 8**: Demonstrative case (#30) sagittal (A) and coronal (B) T1+gadolinium MRI scan of intra-operative imaging from Medtronic VISUALASE system that shows how the thermal damage estimation (TDE, orange contour) didn't completely encompass the lesion – there is a lateral and frontal contrast-enhancing lesion that is was not covered by the TDE. This patient had a local failure after 4 months.

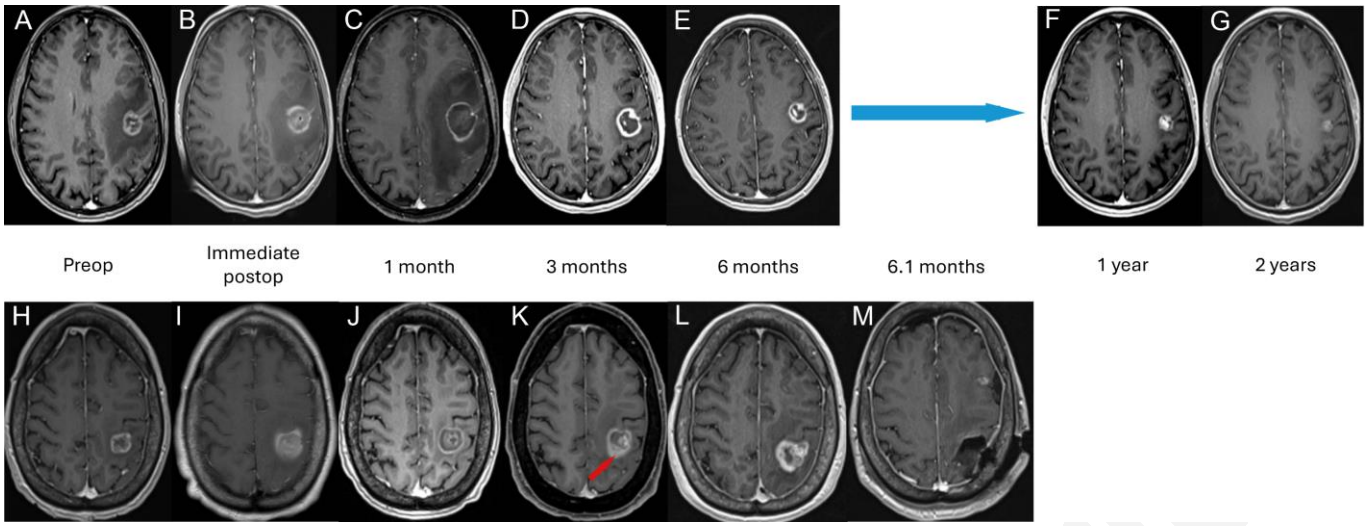

**A.** MRI Cross-Sections with TDE Marks

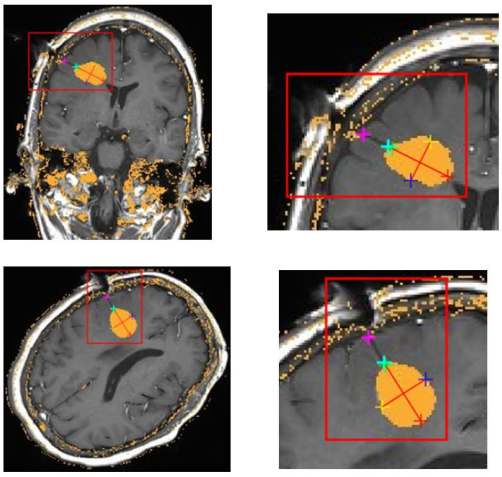

**B.** MRI Cross-Sections Aligned at the Canula

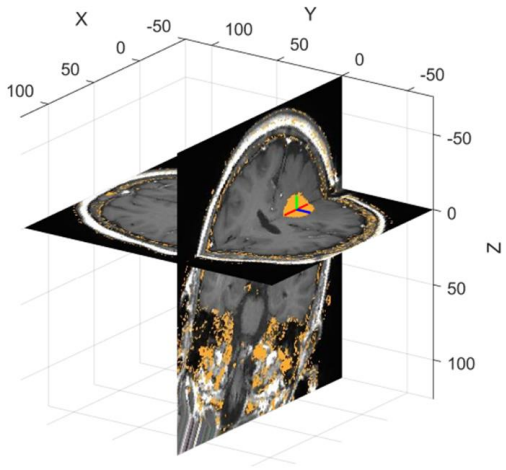


**C.** TDE Cross-Sections Aligned

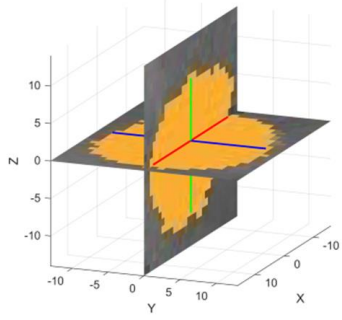

**D.** Ellipsoid Method

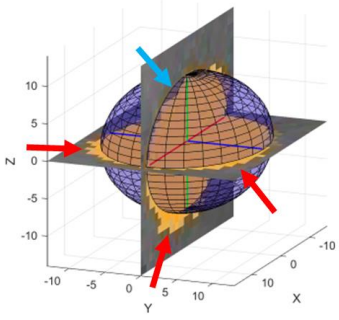

**E.** Liang *et al*. Method using $a_{avg}$

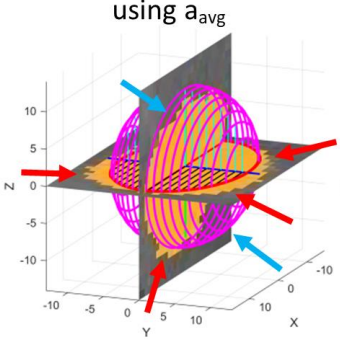

**F.** Liang *et al*. Method using $a_{max}$

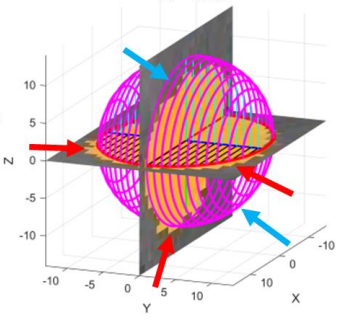

**G.** Quarters Method: Cross-Section (illustration)

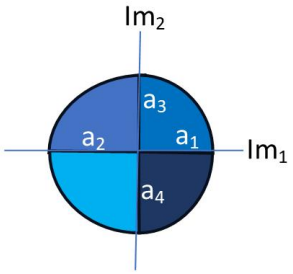


**H.** Quarters Method: Viewpoint I

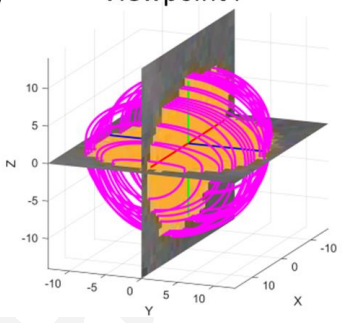

**I.** Quarters Method: Viewpoint II

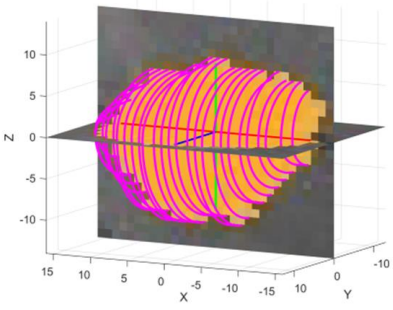

**J.** Quarters Method: Viewpoint III

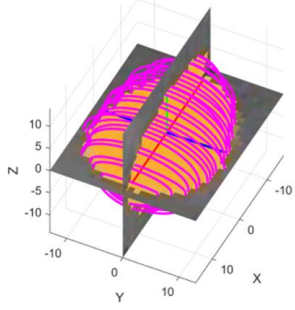

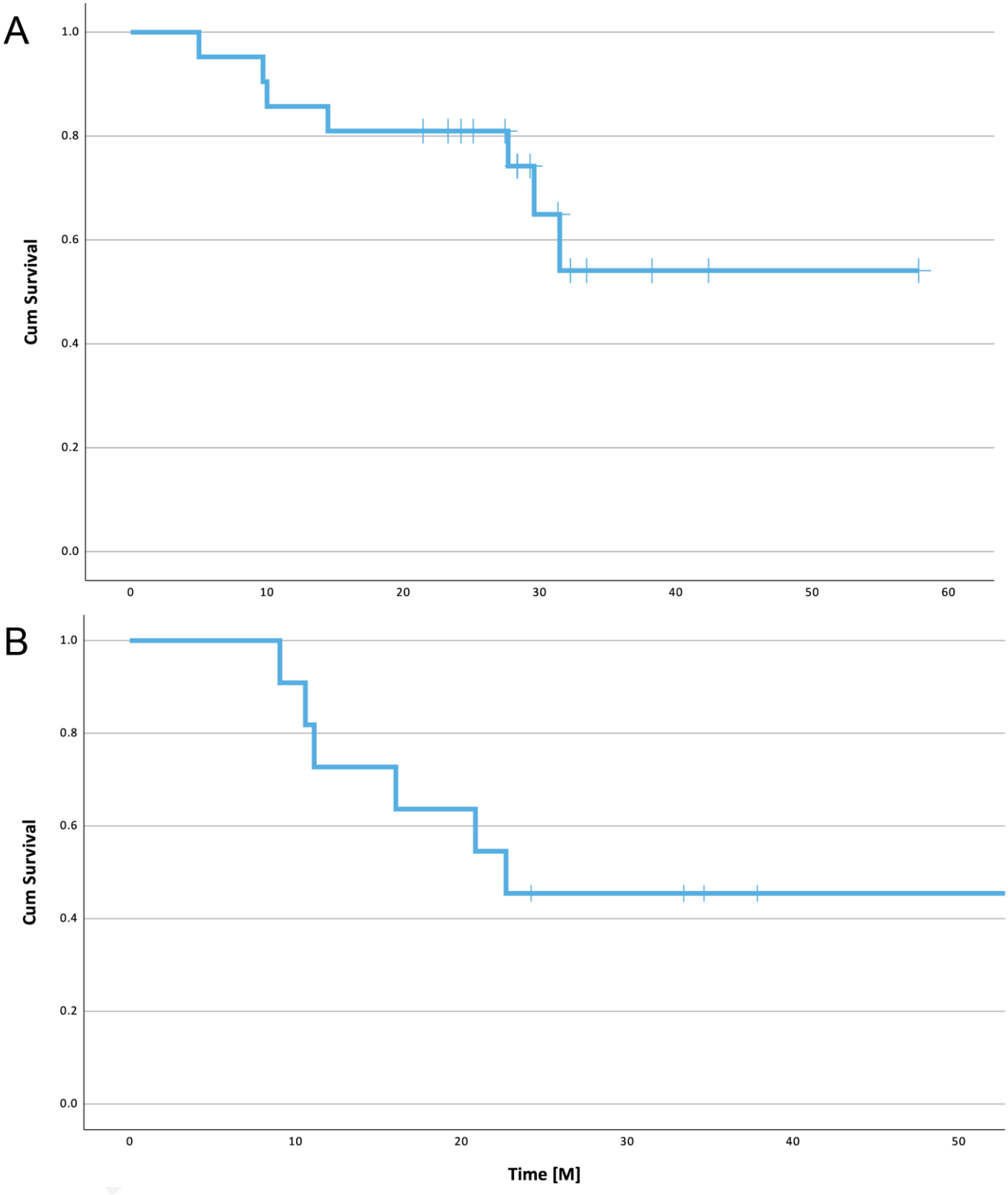

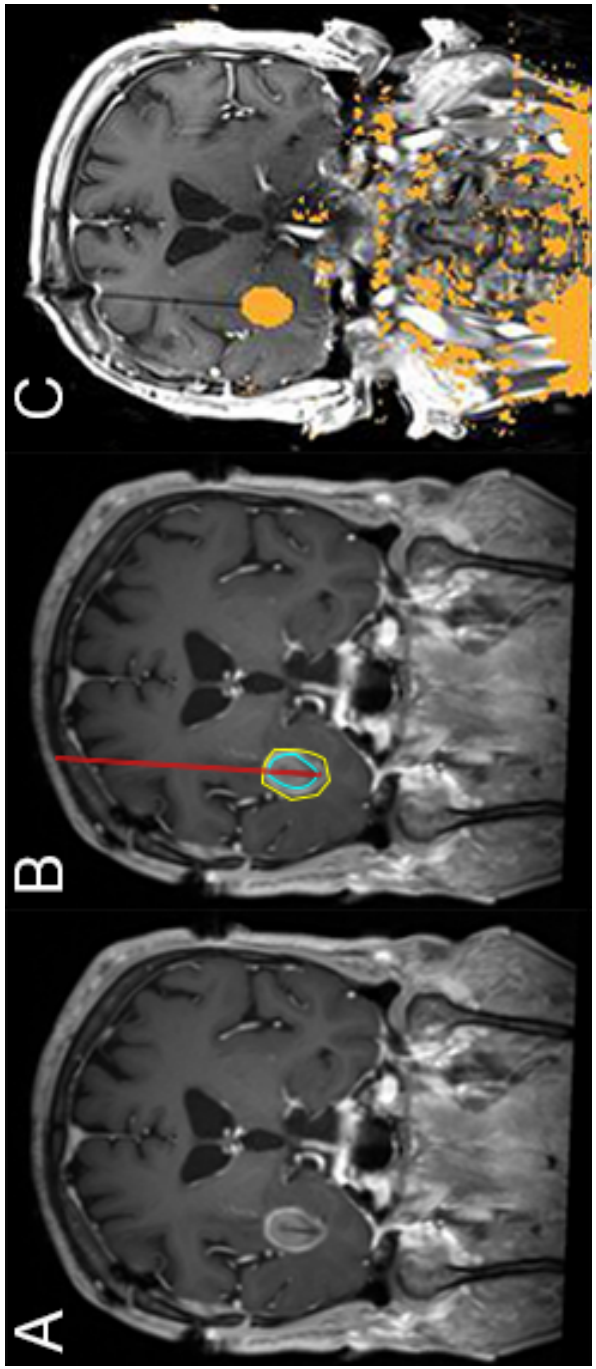

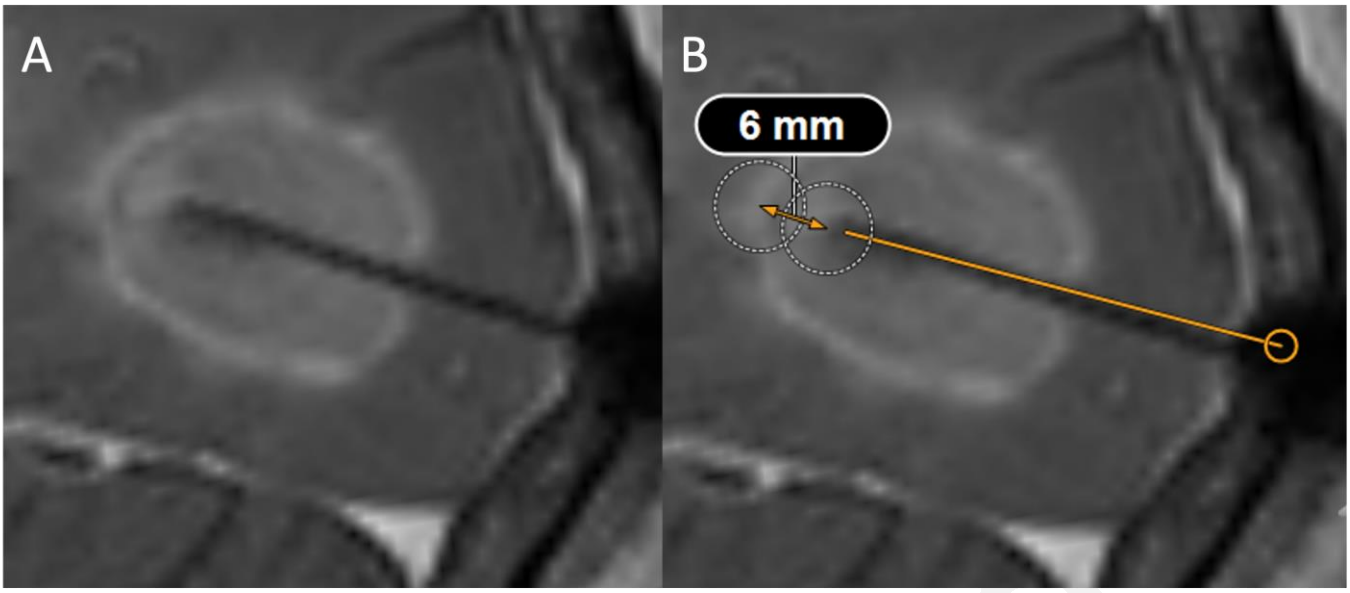

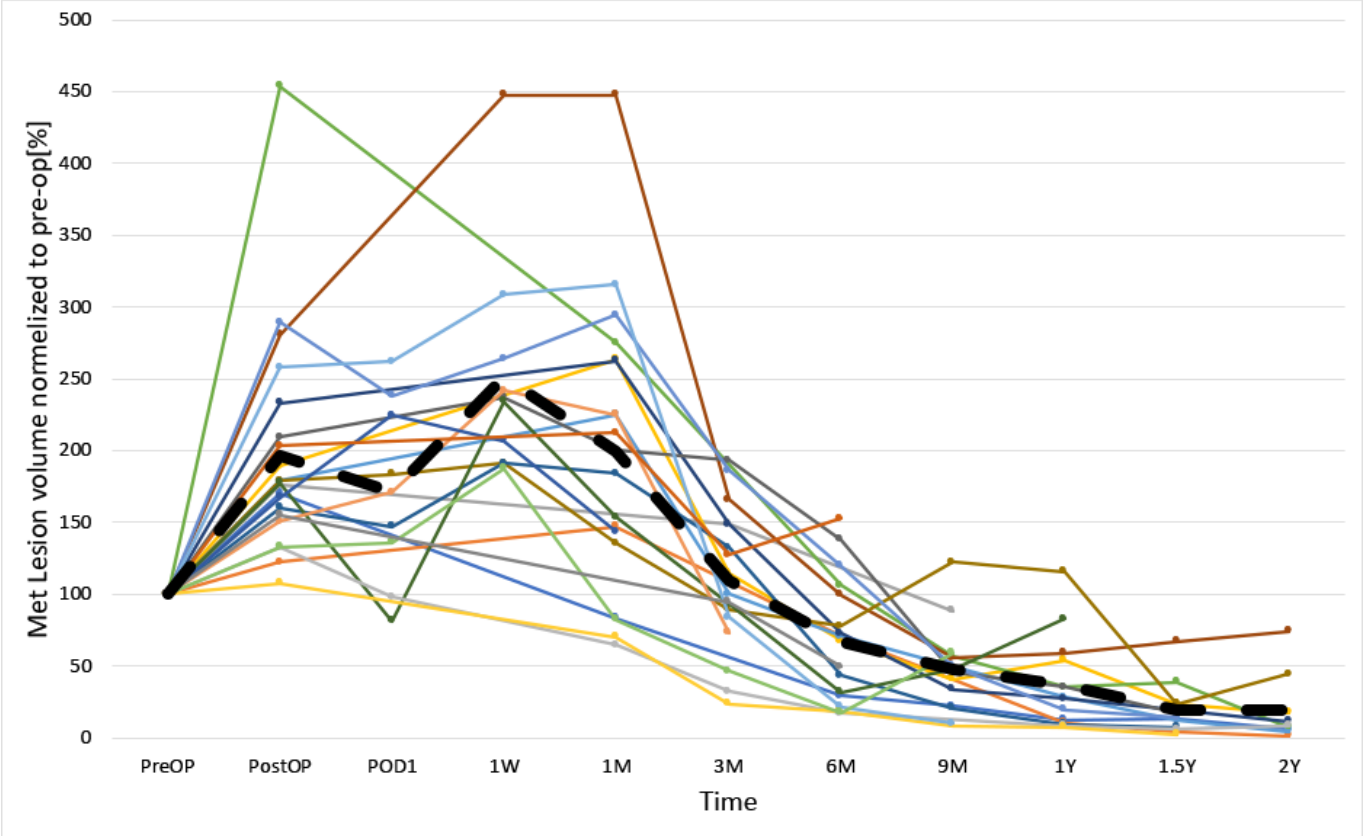

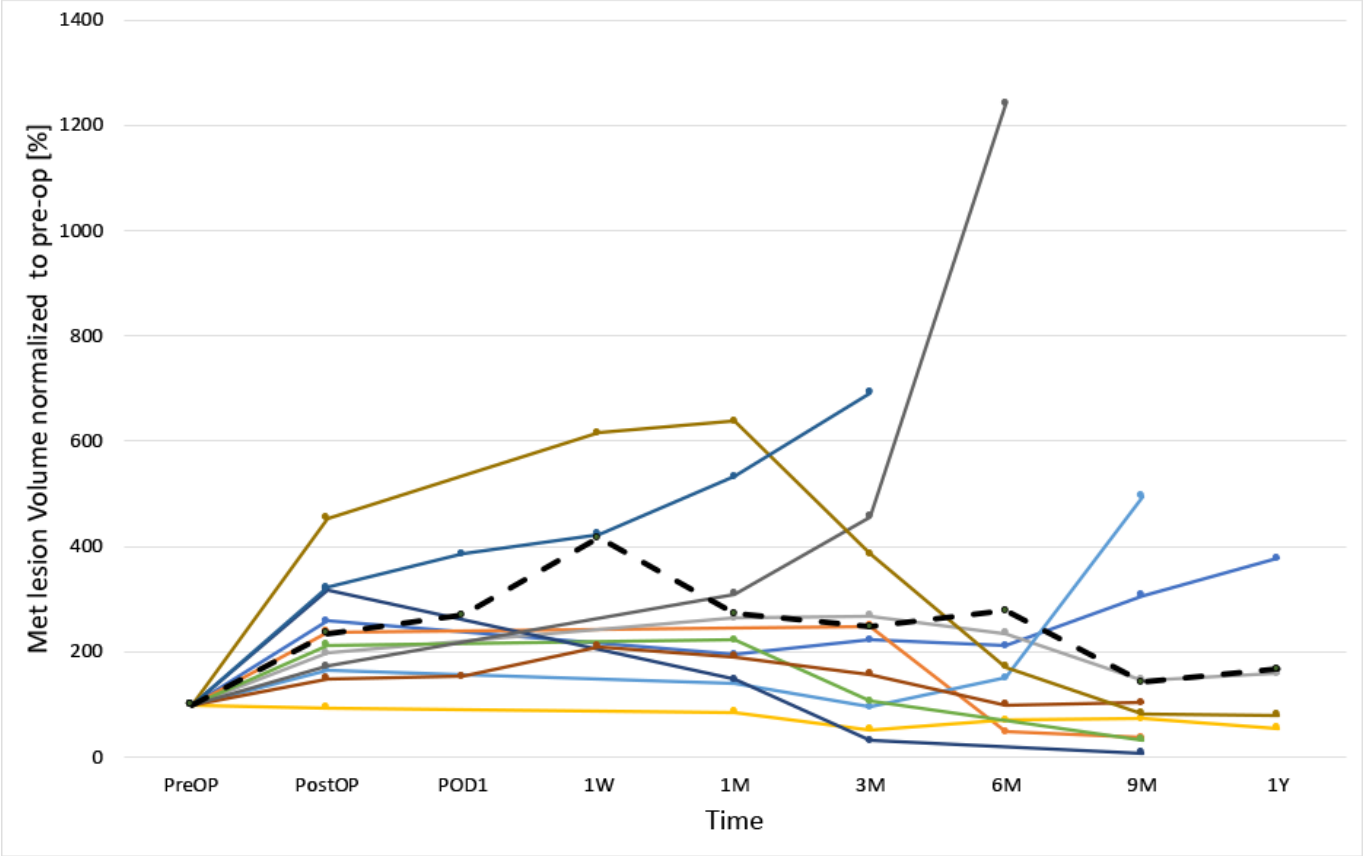

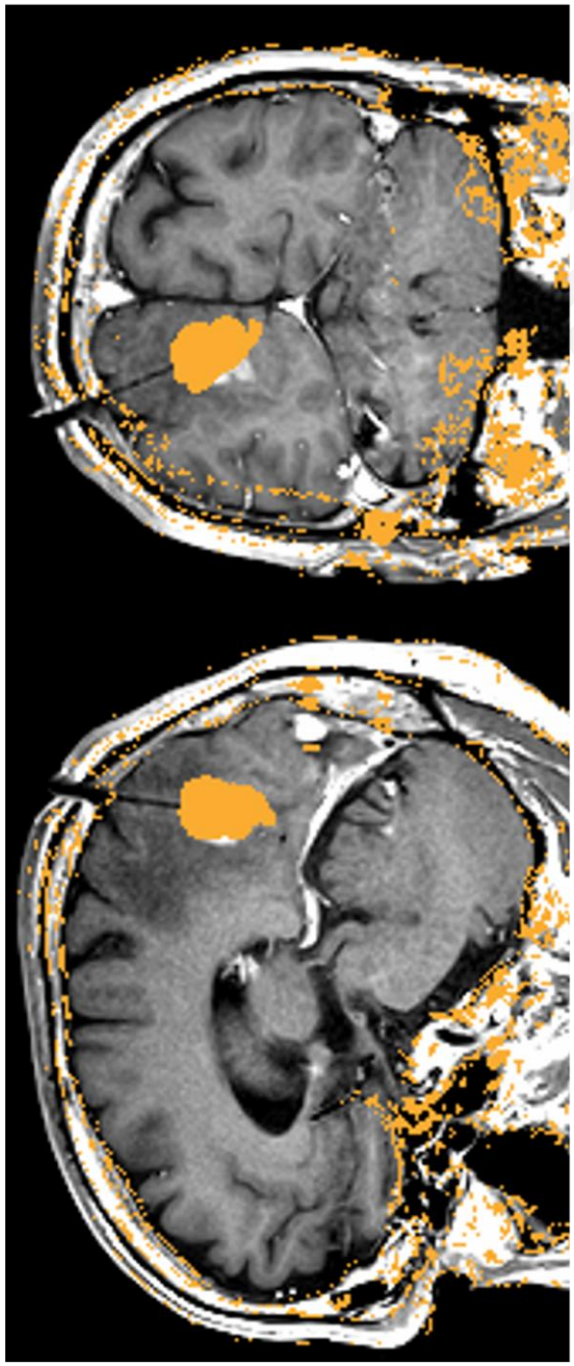

# Imaging changes and clinical outcome after MR-guided Laser Interstitial Thermal Therapy

Table 1: Patient demographics and clinical data

| N | Metastasis Vs. Glial | Original Patology | Side | Location | Lesion pre-op volume [cc] | Lesion max diamter [mm] | Radiology FU Time [m] | Time Local faliure | Survival [M] |
|---|---|---|---|---|---|---|---|---|---|
| 1 | Glial | Oligodendroglioma, WHO2 | Lt | Insular | 0.9 | 16 | 55.3 | 3.4 | 57.60 |
| 2 | Glial | GBM, WHO4 | Rt | Insular | 1.15 | 12.5 | 8.5 | | 11.11 |
| 3 | Met | IDC, ER neg, PR neg, Her2 positive | Rt | Temporal | 2.04 | 18.3 | 57.5 | | 57.8;c |
| 4 | Met | NSCLC, TTF1 pos, EGFR wt, ALK/ROS neg, PDL1>50% | Lt | Temporal | 1.36 | 13 | 26.9 | | 29.59 |
| 5 | Met | NSCLC, TTF1 part pos, P40 neg | Rt | Occipital | 4.76 | 23.3 | 9.1 | | 14.47 |
| 6 | Met | NSCLC, EGFR pos | Lt | Frontal | 1.48 | 14.5 | 25.1 | | 27.68 |
| 7 | Glial | Anaplastic oligodendroglioma, WHO3 | Rt | Periventricular | 1.09 | 12 | 12.5 | | 22.68 |
| 8 | Met | NSCLC, TTF1 pos | Rt | Occipital | 1.2 | 13 | 42.3 | | 42.38; c |
| 9 | Met | NSCLC, TTF1 pos | Lt | Frontal | 1.6 | 14 | 25.4 | | 31.46 |
| 10 | Met | IDC, ER neg, PR neg, Her2 positive | Lt | Frontal | 2.4 | 19 | 35.2 | | 38.24;c |
| 11 | Glial | Astrocytoma WHO3 IDH wt, MGMT nm | Lt | Insular | 5.93 | 18.7 | 37.2 | | 37.84;c |
| 12 | Glial | GBM IDH wt, MGMT nm | Rt | Parietal | 4.7 | 22.1 | 10.2 | 15.5 | 16.04 |
| 13 | Glial | Astrocytoma WHO2 IDHmut, 1p19q intact | Lt | Parietal | 1.21 | 11.7 | 27.7 | | 34.62;c |
| 14 | Met | RCC clear cell | Rt | Frontal | 1.81 | 14.1 | 32.9 | | 33.44;c |
| 15 | Glial | Pilocytic astrocytoma, WHO2 | Rt | Insular | 2.83 | 13.3 | 18.0 | | 33.4;c |
| 16 | Met | SCLC ED | Lt | Parietal | 2.9 | 16.8 | 28.8 | 5 | 32.25;c |
| 17 | Met | IDC, ER neg, PR neg, Her2 positive | Lt | Cerebellar | 2.4 | 17.8 | 28.3 | 6.4 | 31.33;c |
| 18 | Glial | GBM, IDH1 ng, WHO4 | Lt | Temporal | 7.9 | 22.6 | 7.7 | 4.8 | 20.84 |
| 19 | Met | IDC, TP | Rt | Frontal | 1.36 | 13.2 | 28.1 | | 29.29;c |
| 20 | Glial | GBM, IDH WT, MGMT methylated, WHO4 | Rt | Occipital | 2.5 | 14.4 | 8.6 | 2.9 | 9.04 |

| | | | | | | | | | |
|---|---|---|---|---|---|---|---|---|---|
| 21 | Met | IDC, ER neg, PR neg, Her2 positive | Lt | Cerebellar | 5.6 | 21.5 | 25.3 | 3.2 | 28.37;c |
| 22 | Met | SCLC ED | Rt | Basal Ganglia | 0.92 | 13 | 24.9 | | 28.34;c |
| 23 | Met | IDC, ER pos | Rt | Frontal | 4 | 20.5 | 3.8 | | 5 |
| 24 | Met | NSCLC, PDL1 neg, KRAS neg | Lt | Cerebellar | 6.7 | 21 | 25.9 | | 27.45;c |
| 25 | Met | RCC clear cell | Rt | Parietal | 3.16 | 20.9 | 24.6 | | 25.12;c |
| 26 | Met | RCC | Lt | Frontal | 1.54 | 14 | 20.9 | | 24.23;c |
| 27 | Glial | GBM, WHO4 | Lt | Frontal | 1.18 | 11.7 | 13.5 | | 24.2;c |
| 28 | Met | Thyroid | Rt | Parietal | 2.6 | 18 | 6.2 | | 23.28;c |
| 29 | Met | Colon, SATB2 | Lt | Frontal | 4.1 | 16.5 | 6.5 | 3.5 | 21.44;c |
| 30 | Met | NSCLC, TTF pos | Rt | Parietal | 4.3 | 19 | 9.4 | 3.9 | 10 |
| 31 | Met | Melanoma, BRAF neg | Lt | Cerebellar | 2.34 | 15.3 | 4.5 | | 9.7;c |
| 32 | Glial | GBM, WHO4 | Rt | Frontal | 2.27 | 14.2 | 7.0 | 3 | 10.6 |

Table 1: Original pathology refers to the known pathology before the surgery, as biopsies were not performed in our study. Glioblastoma[GBM], Invasive ductal carcinoma[IDC], Non-small cell lung cancer[NSCLC], Renal cell carcinoma[RCC], Small-cell carcinoma[SCLC]; Survival = time in months to mortality or until censored (c, if still alive at last follow-up).